JMEPEG
https://doi.org/10.1007/s11665-018-3574-5

1059-9495/$19.00

Thermo-Fluid Modeling of Selective Laser Melting: Single-Track Formation Incorporating Metallic Powder

Subin Shrestha, Santosh Rauniyar, and Kevin Chou

(Submitted April 29, 2018)

Selective laser melting (SLM) utilizes a laser source to melt and fuse metallic particles to form dense solid parts. Since molten metals have surface tension gradients, the thermo-capillary effect becomes a driving force of melt flow, which will subsequently determine the molten/solidified track as well as the build surface morphology. In this study, a 3D volume of fluid model has been developed to simulate heat transfer and fluid dynamic during single-track laser scanning. A sequential powder addition algorithm is applied to obtain random powder distribution over a thick substrate. Temperature-dependent thermo-physical properties of Ti-6Al-4V are used to define the material, and a volumetric heat source is included as an approximation to laser irradiation. As a result of continuous melting and solidifying, the thermal behavior, the molten metal flow and the free surface formation can be numerically analyzed. In addition, a two-layer simulation has been carried out to study the interlayer bonding. Simulations results are compared with SLM experiments using the single-track morphology acquired by white-light interferometry. The melt pool widths obtained from simulations are in good agreement with the measured single-track widths. On the other hand, it is observed that single tracks formed in SLM have an elevated bead height, which is not realized numerically.

Keywords additive manufacturing, modeling and simulation, powder size distribution, selective laser melting

1. Introduction

Selective laser melting (SLM) is an additive manufacturing (AM) process which utilizes laser source to melt the powder layers. Computer-aided design (CAD) data are decomposed into numerous layers based on the layer height, and each layer is formed by multiple overlapping scan vectors. During each scan vector, as laser irradiates the powder particle, it melts the powder as well as previously deposited layers forming a melt pool within which the flow occurs. As the laser moves, the single track is formed due to solidification in the wake of the laser beam.

The property of single track would determine the final part quality. Each track is formed due to melting through heat transfer, fluid flow and solidification, and the track quality depends on the energy density applied. Hence, the effect of varying energy density on the formation of single track needs to be investigated as the end parts of SLM process are highly dependent on the process parameters selected and it is always desired to optimize the process parameters. To achieve this, numerous experimental studies have been performed (Ref 1, 2). Depending on the process parameters, the resultant single tracks may have different forms: continuous track with a crescent or elliptical section, discontinuous which may be irregularly broken or balled or only partially melted (Ref 3). If the energy density is not enough, balling phenomenon is observed which occurs due to lower wetting ability and is dominant for lower laser power and higher scanning speed (Ref 4, 5). These single scan track experiments help narrow down the process parameter window that would result in dense part and good surface finish.

Single-track experiment helps distinguish appropriate process parameters that would result in dense single tracks without any balling or partial melting. However, thermo-fluid modeling would help understand the inherent fluid flow that leads to the formation of single track. Combined experimental and simulation study is desirable as the simulation helps explain what is happening during experimentation which may otherwise be unknown. If the energy density is very high, evaporation occurs, which results in keyhole formation and keyhole pores. If the energy density is very low, then discontinuous scan tracks are formed as a result of balling formation. These transitions can be studied through thermo-fluid simulations which would assist experimental study to understand and develop process window. However, SLM being powder-bed process, powder particles need to be properly modeled as it would affect the heat transfer as well as fluid flow. Hence, several studies have been focused on mesoscopic modeling of SLM process. Khairallah and Anderson (Ref 6) developed a powder scale model which was able to predict the free surface formation while using constant surface tension. But, it is important to consider Marangoni effect and Lee and Zhang (Ref 7) developed a 3D thermo-fluid model using commercial Flow-3D software incorporating surface tension gradient. Back-and-forth two-track simulation was performed, and the simulation result has been compared with after two-track experiment. Similar modeling approach has also been applied to predict the effect of powder layer thickness on the single-track formation (Ref 8). Khairallah

---

This article is an invited paper selected from presentations at the symposium "Modeling and Simulation in Additive Manufacturing: Materials Design, Property Prediction and Process Control," held during MS&T'17, October 8-12, 2017, in Pittsburgh, Pa., and has been expanded from the original presentation.

Subin Shrestha, Santosh Rauniyar, and **Kevin Chou**, Additive Manufacturing Research Center, University of Louisville, Louisville, KY 40292. Contact e-mail: s0shre03@louisville.edu.

et al. (Ref 9) performed high-fidelity modeling including complex physical phenomenon and elaborated the mechanisms of pore formation, spatter and denudation zones. As the melt pool temperature often exceeds the boiling temperature, it is important to consider recoil pressure as well. Wu et al. (Ref 10) demonstrated the difference in melt pool depth prediction with and without using recoil pressure. If the recoil pressure is ignored, then the depth of the melt pool is underpredicted which is not desirable.

SLM is a layer-upon-layer process, and therefore, the effect of additive layer toward the part formation should also be studied. This would be possible through mesoscopic model when a layer of powder is added to previously scanned layers. Panwisawas et al. (Ref 11) used a simplified powder scale model to understand the behavior of fluid flow toward the formation of pores due to the insufficient melting of powder particles. In addition, build surface formation as well as surface roughness can be predicted more accurately by using powder scale model. However, it would incur a high computational cost to perform area scanning with powder scale model; therefore, studies have been limited to continuum models. Dai and Gu (Ref 12) developed a two-phase continuum model to predict build surface formation at different process parameters. In a similar manner, three-phase model has also been developed for powder-bed electron beam additive manufacturing (PB-EBAM) process (Ref 13).

In this study, a sequential addition algorithm was used to obtain the powder distribution over the base plate. A 3D volume of fluid (VOF) model was developed to predict the heat transfer, fluid flow and resulting track morphology during single-track formation. The transport phenomenon in the melt pool is investigated to understand the formation of a single track during SLM process. In addition, a layer addition algorithm is developed and multilayer simulation is performed.

2. Numerical Modeling

2.1 Powder Scale Model

A 3D model was developed with domain size 1200 μm × 400 μm × 250 μm as shown in Fig. 1. Powder particles are defined by using sequential powder addition algorithm (Ref 14) with some modifications to the reported formulas (Eq 1-3). When a powder particle drops, there may occur four situations: (a) a falling sphere rolls over previously settled sphere, (b) falling sphere rolls over two previously settled spheres, (c) falling sphere becomes stable after being in contact with three spheres, and (d) sphere is not stable even if in contact with three sphere and has to roll further down to stabilize. The algorithm has been discussed in detail in the literature (Ref 14), and only case (a) is shown in Fig. 1 due to the modification made to the powder position update formula. Point B in Fig. 1 represents the contact point between spheres 1 and 2, and point O is the center of sphere 1 which is the reference for the coordinate system. Equations 1-3 represent the change in position of sphere 1 (x_1, y_1, z_1) while rolling down sphere 2 (x_2, y_2, z_2) due to the change in zenith angle θ represented by $\delta\theta$.

$$x_1 = x_2 + (r_1 + r_2) \cdot \sin(\theta + \delta\theta) \cdot \sin\phi \quad \text{(Eq 1)}$$

$$y_1 = y_2 + (r_1 + r_2) \cdot \sin(\theta + \delta\theta) \cdot \cos\phi \quad \text{(Eq 2)}$$

$$z_1 = z_2 + (r_1 + r_2) \cdot \cos(\theta + \delta\theta) \quad \text{(Eq 3)}$$

where r_1 and r_2 are the radius of spheres 1 and 2, respectively, and ϕ is the azimuth angle.

The above-mentioned algorithm has been applied to obtain random powder distribution which would represent the powder-bed condition. In this study, powder size distribution from 15 to 40 μm has been considered and the particles are defined over the 90-μm solid Ti-6Al-4V substrate as shown in Fig. 2. Volume fraction in Fig. 2 differentiates two materials: Ti-6Al-4V and argon. Ti-6Al-4V is defined by volume fraction 1, while argon has volume fraction zero and the free surface has volume fraction in between 0 and 1 and therefore represented by green color. To properly capture the volume fraction, a hexahedral mesh is defined over the domain. Mesh size of 5 μm has been used. The powder particles generated by sequential addition algorithm were read through FLUENT user-defined function (UDF).

2.2 Governing Equations

Laser heat source has been modeled as the conical volumetric heat source which is represented in Eq 4.

$$\dot{Q}_{(x,y,z)} = \eta \times \frac{H_s \times I_z}{S} \quad \text{(Eq 4)}$$

where

$$I_z = \frac{1}{0.75}\left(-2.25\left(\frac{z}{S}\right)^2 + 1.5\left(\frac{z}{S}\right) + 0.75\right),$$

$$H_s = \frac{2P}{\pi d^2}\exp\left\{-\frac{2\left[(x-x_s)^2 + (y-y_s)^2\right]}{d^2}\right\}.$$

Here η represents absorption efficiency, P is laser power, S represents penetration depth, d is beam diameter, and x_S and y_S are heat source center positions. H_s and I_z are horizontal Gaussian distribution heat source and heat source magnitude decaying function in the vertical direction, respectively. The

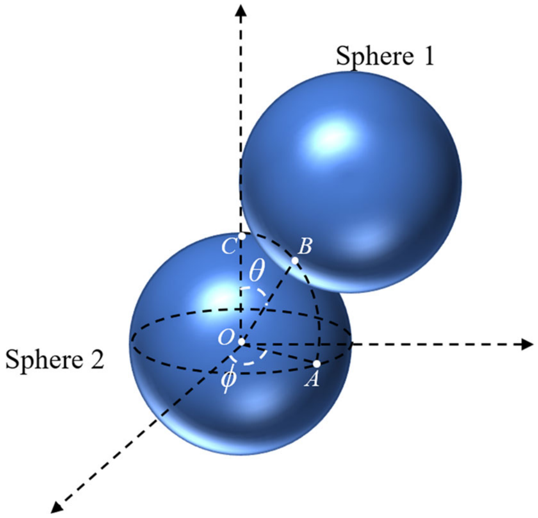

Fig. 1 Incoming sphere rolling down over the previously deposited sphere

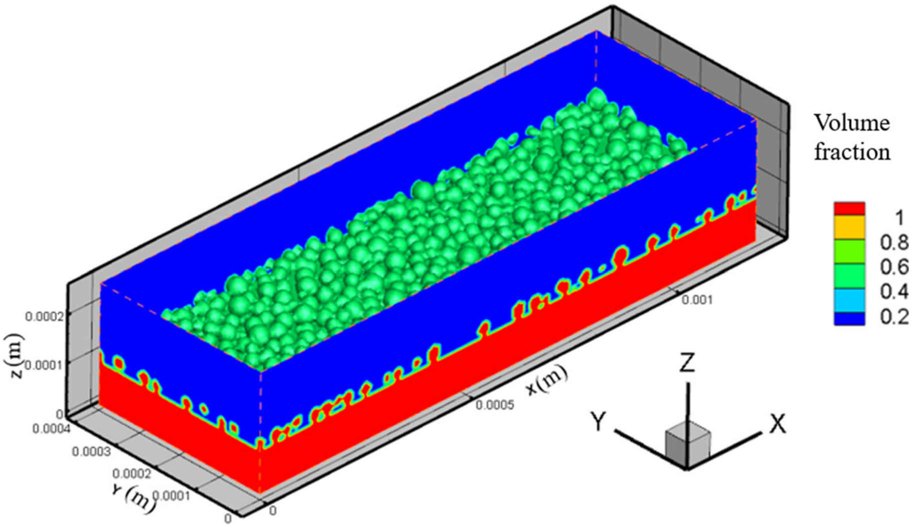

Fig. 2 Computational domain with powder particles distribution used for simulation

heat source is defined in the UDF and applied as the source term in the energy equation. The laser source is moved by updating x_S and y_S positions based on the scanning speed.

2.3 Tracking of Free Surface

The VOF equation which is used to track the free surface during melting and solidification is given as

$$\frac{\partial F}{\partial t} + \vec{v} \cdot \nabla F = 0 \qquad \text{(Eq 5)}$$

where F represents the volume fraction and $\vec{v}$ represents the velocity vector. In this model, two phases have been used: argon as phase 1 with volume fraction 0 and Ti-6Al-4V as phase 2 with volume fraction 1. A free surface of the powder which interacts with the argon has the volume fraction between 0 and 1. VOF equation is solved along with mass, momentum and energy equations.

2.4 Boundary Conditions

The boundary condition at the interface is given as

$$\frac{\partial(\rho H)}{\partial t} + \frac{\partial(\rho u_i H)}{\partial x_i} = \frac{\partial}{\partial x_i}\left(k\frac{\partial T}{\partial x_i}\right) + \dot{Q}(x,y,z) - hA(T - T_\infty) - \sigma A \varepsilon (T^4 - T_\infty^4) \qquad \text{(Eq 6)}$$

where H is the enthalpy, k is thermal conductivity, $\dot{Q}_{(x,y,z)\mathrm{int}}$ is the heat source applied at the interface, h is the heat transfer coefficient, σ is the Stefan–Boltzmann constant and ε is the emissivity which is used to account for the radiation through the top surface and A is the free surface area of cell. Besides the free surface, all the walls in the domain have adiabatic boundary conditions.

2.5 Application of Volumetric Heat Source

In the mesh-based simulation, the free surface should be properly identified in order to appropriately apply the volumetric heat source which is of even more importance due to spherical powder particles. In addition, the surface is continuously deforming during the melting process. Therefore, the topmost cell with nonzero phase 2 volume fraction which is the actual free surface has to be tracked after each iteration which is achieved through UDF. Figure 3 demonstrates how the topmost cell for each column is identified. Volume fraction for each cell in a column is read, and the z-coordinate of each cell, from the same column with volume fraction in the interval (0, 1), is compared. Finally, the topmost cell which is irradiated to the laser is defined as free surface for that column. The arrowhead points to the free surface cell which is pointed for each cell beneath the topmost cell. The free surface cell information is utilized to define the magnitude of heat source for cells beneath based on the penetration depth.

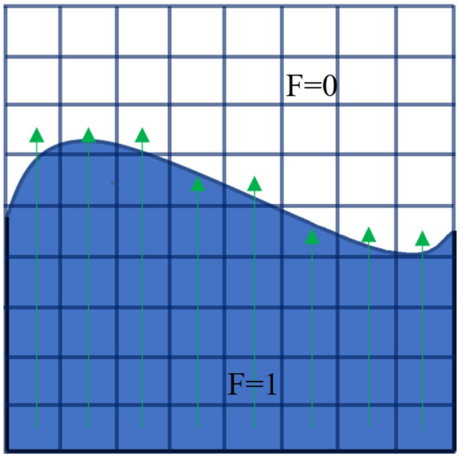

Fig. 3 2D representation of topmost free surface identification to apply a volumetric heat source

2.6 Material Properties

Physical properties such as thermal conductivity, specific heat and density are the function of temperature. Therefore, temperature-dependent material properties summarized in Fig. 4 are used to define solid and powder Ti-6Al-4V. As the properties are almost linear with the temperature, they are defined as piecewise linear in FLUENT. Besides these, surface tension is also the function of temperature. Additional material properties of Ti-6Al-4V are summarized in Table 1. Generally, the surface tension of metal can be defined by Eq 7.

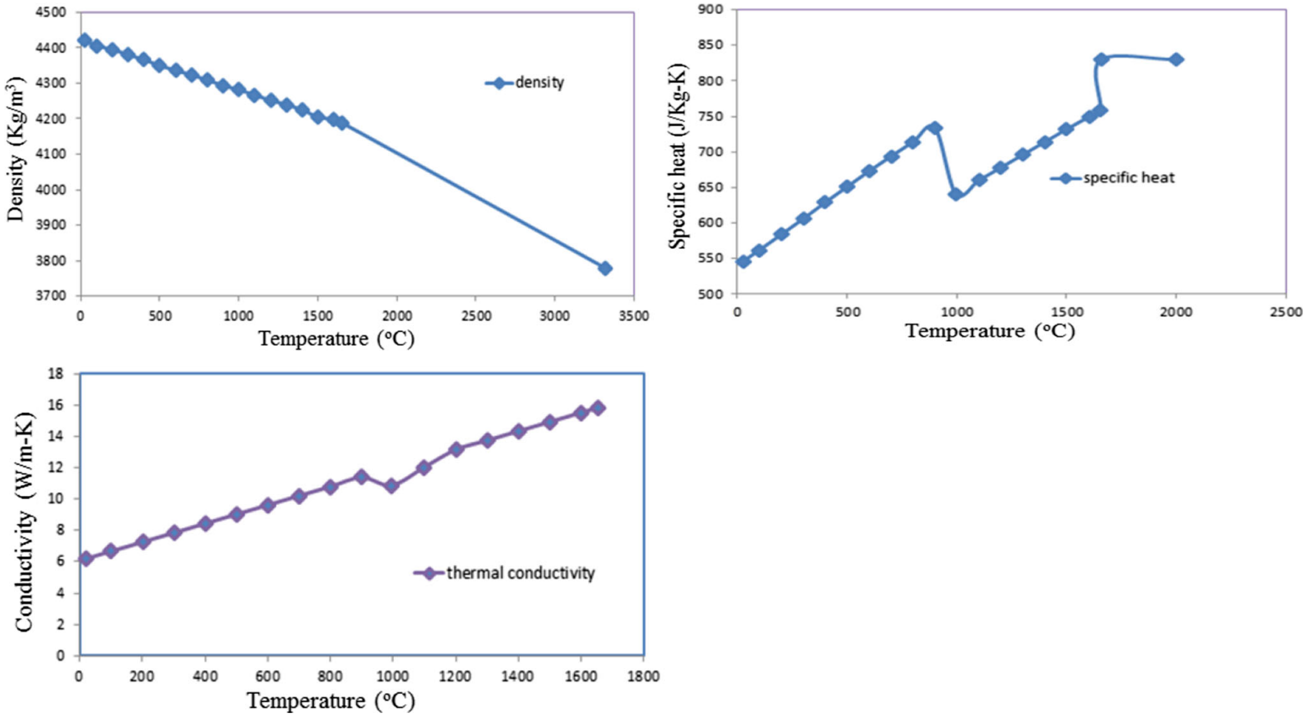

Fig. 4 Temperature-dependent material properties of Inconel Ti-6Al-4V (Ref 13)

$$\gamma = \gamma_m + \frac{d\gamma}{dT}\Delta T \tag{Eq 7}$$

where γ is the surface tension, γ_m is the surface tension at the melting point, $\frac{d\gamma}{dT}$ is the surface tension gradient and ΔT is the temperature difference in reference to the melting temperature.

3. Results and Discussion

3.1 Single-Layer Simulation

3.1.1 Typical Simulation. The result of melt pool flow for scanning speed 600 mm/s and power 195 W is described in this section. When the heat source is not applied, powder particles remain solid. The application of heat source increases the temperature of a certain volume of powder with the highest temperature at the center of the laser beam. With further increase in the temperature, powder particle at the center starts to melt which is then followed by the melting of surrounding powder particles as shown in Fig 5(a). The smaller powder particles would melt before larger powder particles in the powder particles mixture of 15-40 µm. The melted powder fills the void between powder particles due to the continuous flow of liquid, and the melt pool becomes dense. The melt pool solidifies with the progress in time as the heat source moves from left to right. This process of melting and solidification continues to form a single track. The smaller powder will melt rapidly in case of high energy density, and the temperature may exceed the boiling point of the material. This would result in evaporation and result in the higher depression below the heat source. In this calculation, the evaporation is not considered, and the effect of recoil pressure is also not included.

During melting, the flow is outwards, from higher temperature to lower temperature due to surface tension gradient. The heat source is moved from the left to right which allows the rear to cool down due to heat diffusion. During the solidification, the melt flow changes direction from outer flow to inner flow which contributes to the formation of a continuous bead. Figure 6 illustrates the transient behavior of melt flow during

Table 1 Material properties of Ti-6Al-4V

Parameters	Values
Solidus temperature, T_S, °C	1605 (Ref 15)
Liquidus temperature, T_L, °C	1655 (Ref 15)
Latent heat of fusion, L_f , kJ/Kg	440 (Ref 15)
Beam diameter, d, µm	100
Power, W	195
Viscosity, kg/ms	0.049
Emissivity, ε	0.5 (Ref 16)
Stefan–Boltzmann constant, σ	5.67×10^{-8}

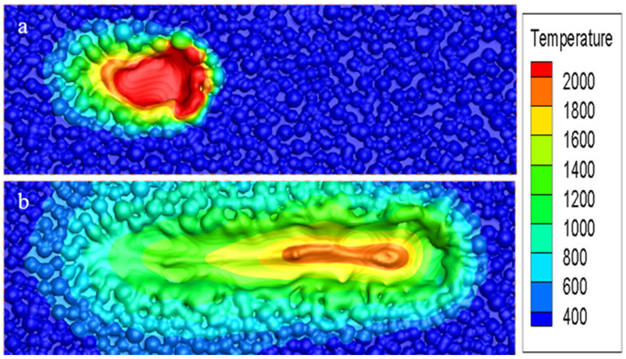

Fig. 5 Top view of the powder bed showing (a) the melt pool at $t = 400$ µs and (b) solidified track at $t = 1600$ µs along with the temperature distribution (°C)

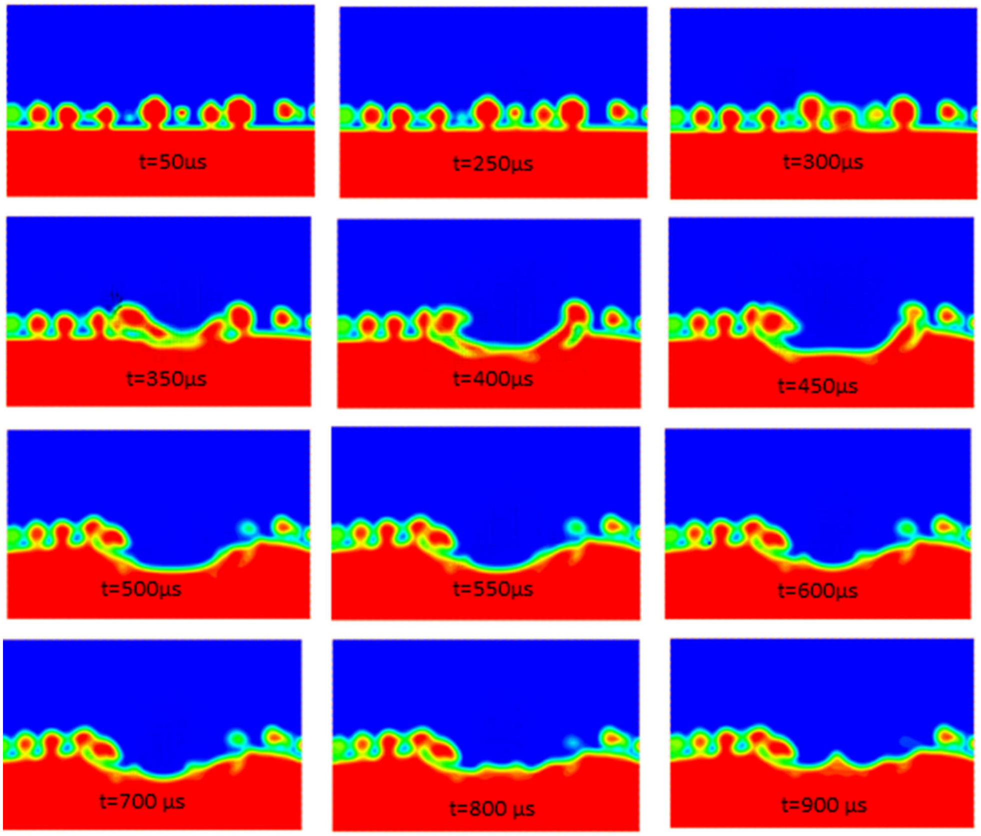

Fig. 6 Melt pool dynamics during melting and solidification

single-track formation. The transverse cross section at 405 μm for scanning speed 600 mm/s with time progression is presented in Fig. 6. These figures represent the volume of fluid fraction. The spherical powder slowly starts to change its shape at *t* = 300 s μs. The melt pool depth keeps increasing up to *t* = 500 μs after which the solidification starts. During the solidification, the melt flow is pulled in the upward direction to form a track as seen in *t* = 900 μs. The powder has been completely melted, and the melt pool depth increases. It clearly shows that the melt pool increases in depth during the heating period, and then, the flow reverses back under the effect of increasing surface tension to form a solid track.

In addition, it is observed that there is a shallow area at the end of the scan track. This may be due to the insufficient flow of melt pool at the end of the scan track. When the laser is turned off, the melt pool immediately solidifies leaving a shallow region at the end of the scan track. As the void region is filled during the solidification, the insufficient melt flow at the beam turnoff point may result in pore formation.

A quick view just after the solidification at the point where the laser is stopped shows that the depth of that shallow region changes according to the scanning speed.

3.1.2 Process Parameter Effect. Power and speed affect the amount of energy being fed into the powder bed which ultimately affect the thermal response as well as melt flow. Therefore, melt pool formed due to change in scanning speed at same power of 195 W is summarized in Fig. 7. We may observe that the melt pool width decreased with increasing speed. This is due to the temperature distribution within the melt pool as low speed result in higher-temperature zones within the melt pool compared to high speed. The melt pool width observed during the simulation with 400, 600, 800 and 1000 mm/s was 220, 200, 160 and 140 μm, respectively.

Single-track experiment was carried out in an EOS M270 machine with TiAl6V4 powder. Four single tracks were formed on the top surface with different scanning speeds 400, 600, 800 and 1000 mm/s at 195 W laser power. Then, formed track surface was analyzed through the white-light interferometer to obtain the melt pool width which is depicted in Fig 8. The 2D cross section has been presented for two cases: 400 and 600 mm/s. The bead height measured is above the layer thickness. At certain cross section, single-track bead height for 400 mm/s was 90 μm, whereas for 600 mm/s it was 80 μm although 30 μm was used during the experiment. Five similar cross sections were taken in a span of 1000 μm from the interferometer and averaged to calculate the track width. Single data were taken from the computational result using Tecplot with an accuracy of 10 μm. The track width value obtained from the experiment follows the trend and is in good agreement with the computational result as shown in Fig. 9.

Figure 10 shows the single-track morphology predicted for different scanning speeds. It is important to note that the single-track morphology is very different considered to the experimental scan tracks. There are several reasons for this difference. During the single-track experiment, the neighbor powder particles get sucked into the melt pool which would add the mass into the single track, therefore increasing the bead height (Ref 17). In addition, the layer thickness after certain height may be more than defined layer thickness to compensate for the shrinkage due to low powder packing density. In this simula-

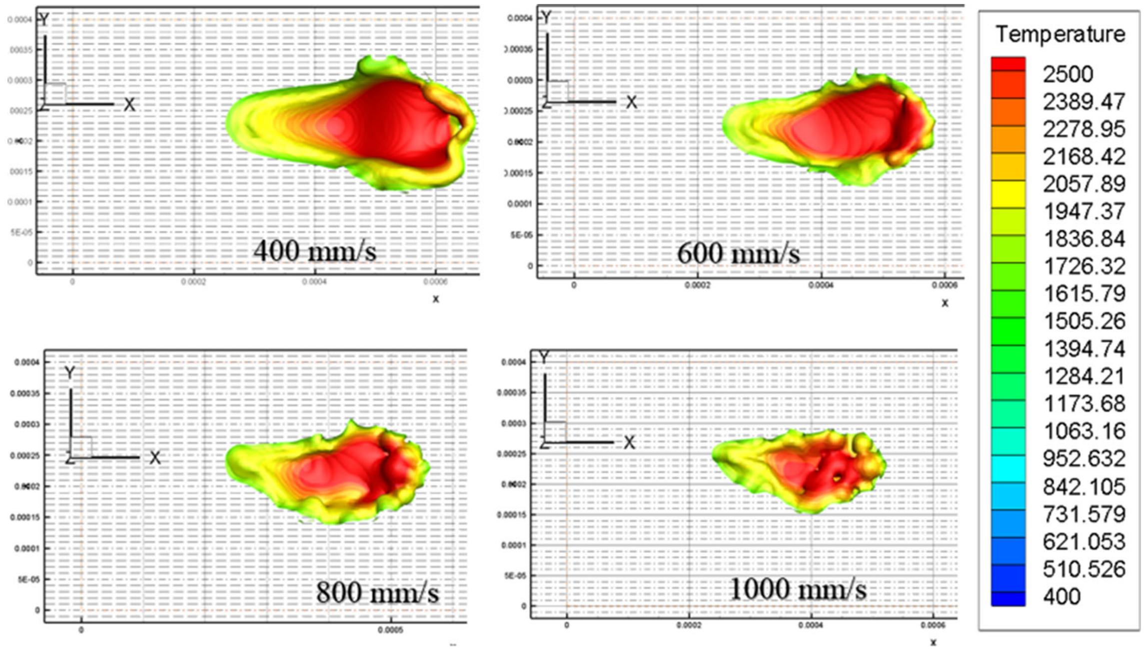

Fig. 7 Melt pool comparison between different process parameters

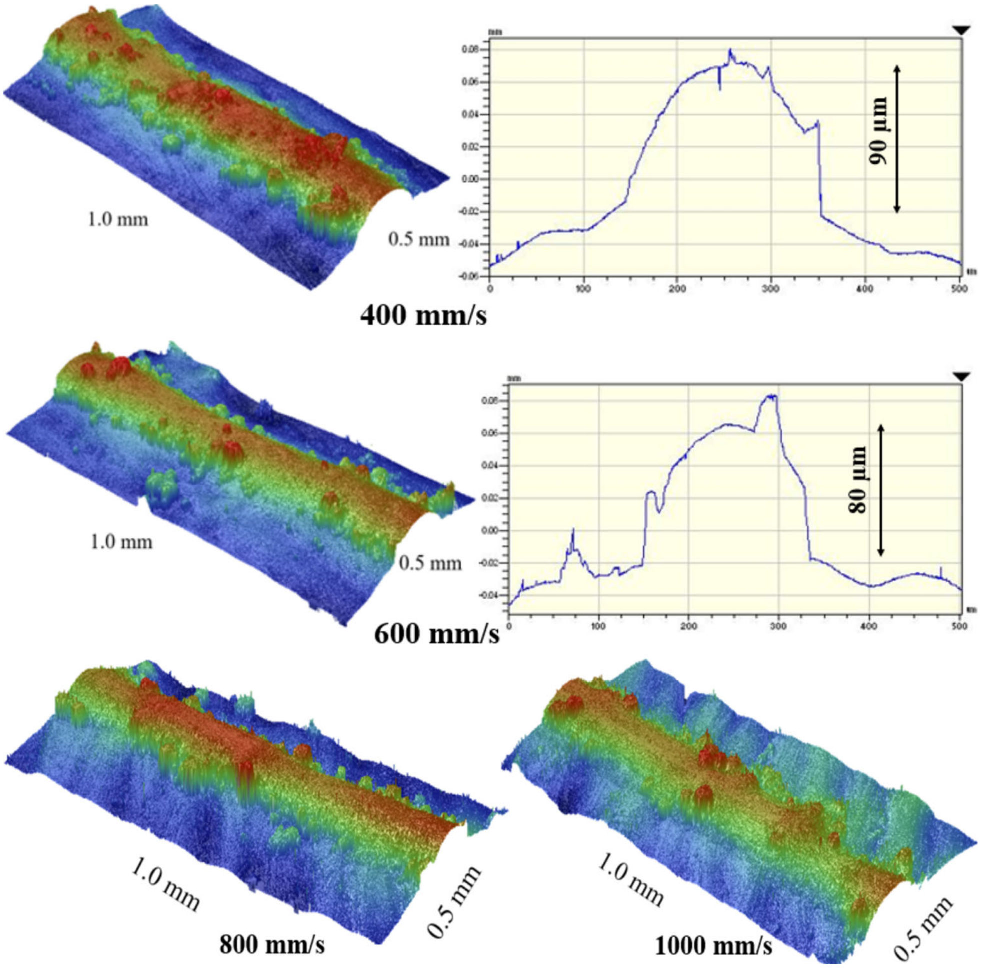

Fig. 8 Surface morphology for four velocity values at a constant power of 195 W

tion, these factors have not been considered, and therefore, very small bead is formed during solidification.

In the SLM process, laser turnoff point is often important as there is often insufficient melt flow due to which pores may occur. Figure 11 helps explain the track end morphology at different scanning speeds. At low speed of 400 mm/s, there may be numerous pores formed at the end of the single track.

3.2 Two-Layer Simulation

SLM is a layer-by-layer process, and therefore, the part quality depends upon the interaction between layers as well. In this prospect, multilayer simulation becomes important. A solidified track from the previous layer would affect the powder particle distribution. Therefore, a two-layer simulation is carried out. To achieve this, at first, one-layer simulation is performed, and after its completion, the free surface, that is single track, and neighbor powder particles are exported as a mesh. A program which was developed based on sequential powder addition algorithm was modified to read the free surface data. Figure 12 shows how the second-layer algorithm works: The powder is dropped from a certain height, and as soon as it comes in contact with the sphere, the stability is checked by reading the neighbor mesh. If the particle is not stable, then the iteration is continued and the particles are rolled down to lower mesh until the particle becomes stable. Moreover, if the incoming sphere comes in contact with a previously deposited sphere, the same algorithm which has been discussed earlier is followed.

Thus, developed second-layer powder addition algorithm was applied to obtain the second layer of powder distributed over the first layer. Figure 13 illustrates the powder being added. We can clearly see from Fig. 13(a) how the first layer is being covered up by second layer, and after the complete addition, the first-layer track is not visible.

For two-layer simulation, higher scanning speed was selected to reduce the computational time; at first, 1000 mm/s scanning speed is used with 195 W power. Figure 14 shows the transient behavior of the free surface during the melting process. It has been experimentally shown that during the scanning process, the melt pool attracts neighbor particles (Ref 17). We may observe similar phenomenon during the simulation as well. Initially, when heat is not applied, second-layer powder particles are settled over the first layer. However, as the

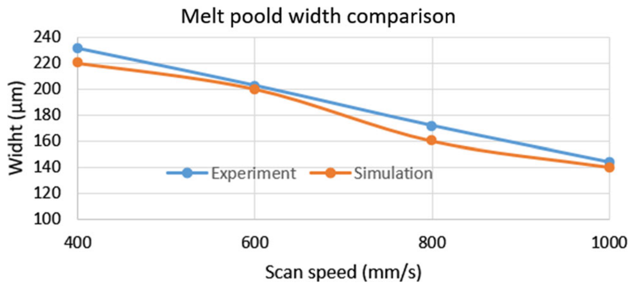

Fig. 9 Melt pool width comparison between experiment and simulation

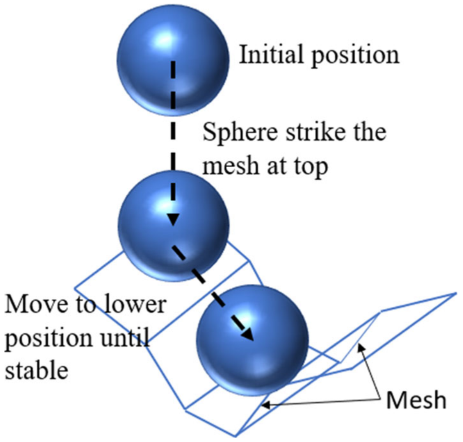

Fig. 12 Second-layer powder addition demonstration

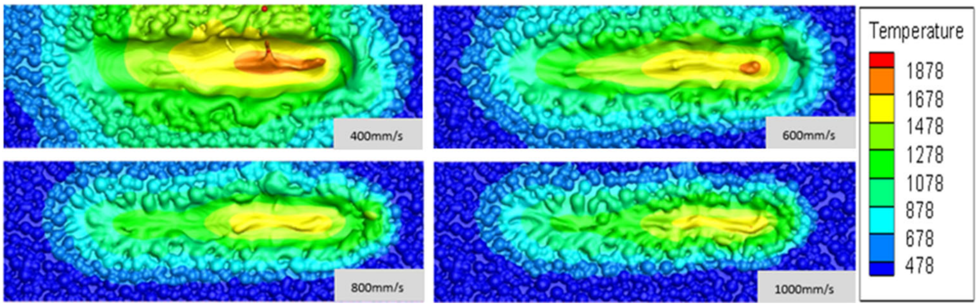

Fig. 10 Solidified single tracks at different scanning speeds

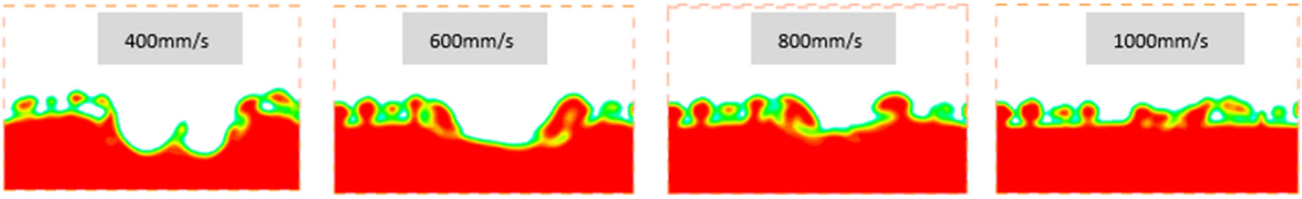

Fig. 11 Image slice of the 3D domain at the shallow region for four scanning speeds

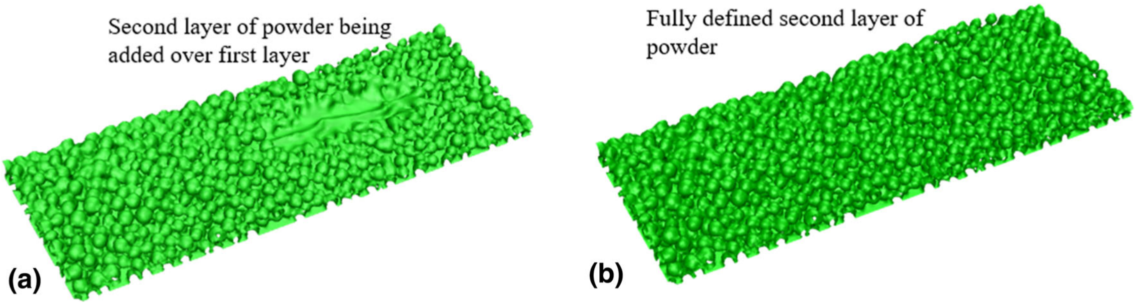

Fig. 13 (a) Second layer of powder being defined over first layer and (b) second layer of powder after fully defined

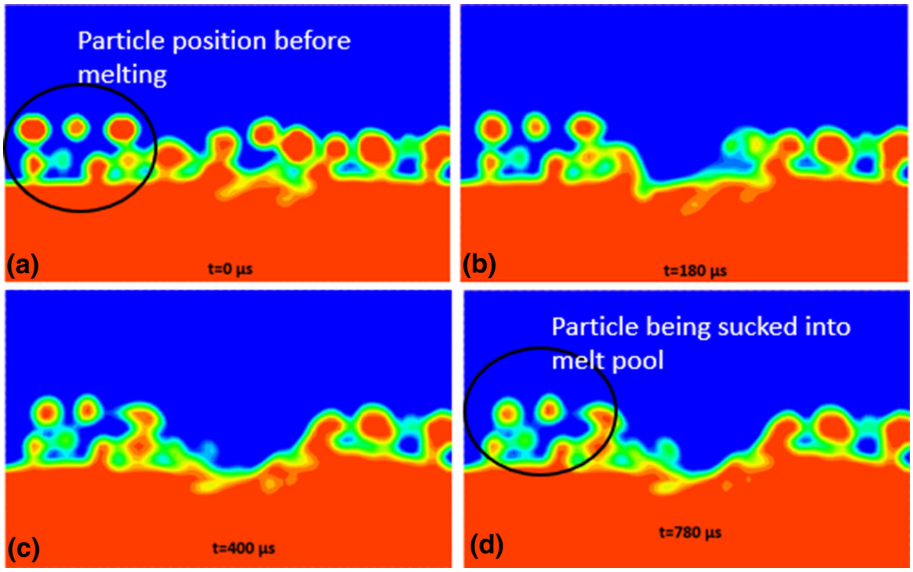

Fig. 14 (a) Solidified single track after second-layer scanning, (b) transverse and (c) longitudinal cross section of solidified two-layer single track (v = 1000 mm/s)

melt pool begins to form, its flow drives in such a manner that the neighbor particles get attracted to the melt pool as well. However, due to the mesh-based simulation, the particles do not get mixed into the melt pool. Due to this limitation, bead formation would not be properly formed in this study.

4. Conclusions

In this study, sequential addition algorithm was adopted to obtain powder-bed distribution over a solid substrate. A 3D thermo-fluid model was developed, and powder particles distribution was imported to study fluid flow during melting and solidification processes. Single-track formation in both single-layer and two-layer depositions was developed to investigate the fluid dynamics in the melt pool and the formation of a single track. Different scanning speeds were tested to study the temperature distribution, fluid velocity and the formation of pores. Based on the simulation results, following conclusions can be made.

- Inside the metal molten pool, the outward flow is observed during the melting process, while the inward flow is observed during the solidifying stage.
- In the testing range, the track width decreases with decreasing the laser scan energy density.
- The single-track bead height from simulations is lower than that observed in the SLM experiments, which is even higher than the layer thickness due to possibly the denudation phenomenon (Ref 9, 17).
- The free surface information from the first-layer single-track simulations can be used to obtain the second-layer powder distribution. Proper interlayer bonding has been predicted for 195 W laser power and 1000 mm/s scanning speed.

Acknowledgment

This research is partially supported by NIST (70NANB16H029) and NSF (1662662).

References

1. J.-P. Kruth, L. Froyen, J. Van Vaerenbergh, P. Mercelis, M. Rombouts, and B. Lauwers, Selective Laser Melting of Iron-Based Powder, *J. Mater. Process. Technol.*, 2004, **149**(1), p 616–622

2. I. Yadroitsev, P. Bertrand, and I. Smurov, Parametric Analysis of the Selective Laser Melting Process, *Appl. Surf. Sci.*, 2007, **253**(19), p 8064–8069
3. T. Childs, C. Hauser, and M. Badrossamay, Mapping and Modelling Single Scan Track Formation in Direct Metal Selective Laser Melting, *CIRP Ann. Manuf. Technol.*, 2004, **53**(1), p 191–194
4. R. Li, J. Liu, Y. Shi, L. Wang, and W. Jiang, Balling Behavior of Stainless Steel and Nickel Powder During Selective Laser Melting Process, *Int. J. Adv. Manuf. Technol.*, 2012, **59**(9–12), p 1025–1035
5. Dilip, J., Anam, M.A., Pal, D., Stucker, B., A Short Study on the Fabrication of Single Track Deposits in SLM and Characterization. In *Proceedings of the Solid Freeform Fabrication Symposium*, pp. 1644–1659
6. S.A. Khairallah and A. Anderson, Mesoscopic Simulation Model of Selective Laser Melting of Stainless Steel Powder, *J. Mater. Process. Technol.*, 2014, **214**(11), p 2627–2636
7. Y. Lee and W. Zhang, Modeling of Heat Transfer, Fluid Flow and Solidification Microstructure of Nickel-Base Superalloy Fabricated by Laser Powder Bed Fusion, *Addit. Manuf.*, 2016, **12**, p 178–188
8. C. Panwisawas, C. Qiu, M.J. Anderson, Y. Sovani, R.P. Turner, M.M. Attallah, J.W. Brooks, and H.C. Basoalto, Mesoscale Modelling of Selective Laser Melting: Thermal Fluid Dynamics and Microstructural Evolution, *Comput. Mater. Sci.*, 2017, **126**, p 479–490
9. S.A. Khairallah, A.T. Anderson, A. Rubenchik, and W.E. King, Laser Powder-Bed Fusion Additive Manufacturing: Physics of Complex Melt Flow and Formation Mechanisms of Pores, Spatter, and Denudation Zones, *Acta Mater.*, 2016, **108**, p 36–45
10. Y.-C. Wu, C.-H. San, C.-H. Chang, H.-J. Lin, R. Marwan, S. Baba, and W.-S. Hwang, Numerical Modeling of Melt-Pool Behavior in Selective Laser Melting with Random Powder Distribution and Experimental Validation, *J. Mater. Process. Technol.*, 2018, **254**, p 72–78
11. C. Panwisawas, C. Qiu, Y. Sovani, J. Brooks, M. Attallah, and H. Basoalto, On the Role of Thermal Fluid Dynamics into the Evolution of Porosity During Selective Laser Melting, *Scr. Mater.*, 2015, **105**, p 14–17
12. D. Dai and D. Gu, Tailoring Surface Quality Through Mass and Momentum Transfer Modeling Using a Volume of Fluid Method in Selective Laser Melting of TiC/AlSi10 Mg Powder, *Int. J. Mach. Tools Manuf.*, 2015, **88**, p 95–107
13. S. Shrestha and K. Chou, A Build Surface Study of Powder-Bed Electron Beam Additive Manufacturing by 3D Thermo-Fluid Simulation and White-Light Interferometry, *Int. J. Mach. Tools Manuf*, 2017, **121**, p 37–49
14. J. Zhou, Y. Zhang, and J. Chen, Numerical Simulation of Random Packing of Spherical Particles for Powder-Based Additive Manufacturing, *J. Manuf. Sci. Eng.*, 2009, **131**(3), p 031004
15. G. Welsch, R. Boyer, and E. Collings, *Materials Properties Handbook: Titanium Alloys*, ASM International, Materials Park, 1993
16. M. Kobayashi, M. Otsuki, H. Sakate, F. Sakuma, and A. Ono, System for Measuring the Spectral Distribution of Normal Emissivity of Metals with Direct Current Heating, *Int. J. Thermophys.*, 1999, **20**(1), p 289–298
17. M.J. Matthews, G. Guss, S.A. Khairallah, A.M. Rubenchik, P.J. Depond, and W.E. King, Denudation of Metal Powder Layers in Laser Powder Bed Fusion Processes, *Acta Mater.*, 2016, **114**, p 33–42